**ORIGINAL PAPER**

# A general approach for controllable surface structuring of metals via through-mask electrochemical micromachining under isotropic etching mode

**Rong Yi**[1] ⬤ · **Muhammad Ajmal Khan**[2] · **Hui Deng**[3]

## Abstract

Surface structuring has attracted growing interest in the industry due to its potential to improve the macroscopic properties of workpieces. This work investigated the surface structuring of metals by combining thermal oxide film mask and laser lithography with isotropic etching. The metals were thermally oxidized to form a protective oxide film, laser ablation patterned the thermal oxide film, while electrochemical etching operated in the isotropic mode obtained an array of hemispherical cavities. The isotropic etching potential for different metals is taken from the mass transport region of the polarization curve. The effects of thermal oxide film thickness and laser ablation area on the uniformity of the etching holes were studied. The thermal oxidation of TA2 at 350 °C formed a 20-nm-thick oxide film, while an array of 10 μm radius hemispherical microcavities was fabricated on the laser patterning surface via electrochemical etching at 2 V for 1 min. The surface structuring of stainless steel, pure nickel, and tungsten is highly dependent on the ability of the oxide film to avoid electrochemical reactions. The feasibility of combining thermal oxidation and laser lithography with electrochemical etching is of great value for the surface structuring of metallic materials for biomedical and microsystem applications.

**Keywords** Surface structuring · Isotropic etching · Laser lithography · Hemispherical microcavities

## Introduction

Surface structuring is a promising technique for microfluidic, micro-optical, and micromechanical applications since fabricating micro- or nano-scale structures design materials with advanced surface properties [1–3]. Direct laser interference patterning (DLIP) offers high flexibility and throughput for surface structuring with feature sizes in the micro and nanoscale [4]. A single laser pulse with energy densities between 0.3 and 5.1 J/cm$^2$ can generate periodic crater or pillar-like patterns on the titanium surface. However, the surface quality of the structures fabricated with laser pulses deteriorates due to the recast layer formation [5].

Electrochemical processes for the surface structuring of metals by controlling anodic dissolution have been developed in recent years [6]. Controlling the anodic dissolution reaction in a confined area with a micron or submicron precision is the key challenge in the surface structuring of metals [7]. Typically, micro- or nano-scale machining tools are needed to achieve nanostructuring of metals [8, 9]. Since electrochemical processes involve no mechanical interaction, no residual stress or tool wear is left after surface structuring. At the same time, it can fabricate structures on metallic materials that are even harder than the tool material [10]. Many variants of electrochemical processes such as pulsed electrochemical machining (PECM), wire-electrochemical machining (Wire-ECM), jet-electrochemical machining (Jet-ECM), and through-mask electrochemical micromachining (TM-ECMM), have been developed to realize metal surface structuring.

✉ Rong Yi
11930903@mail.sustech.edu.cn

✉ Hui Deng
dengh@sustech.edu.cn

1   College of Mechanical Engineering, University of South China, No. 228, Hengqi Road, Hengyang, Hunan 421001, China

2   Department of Mechanical Engineering, George Mason University, Fairfax, VA 22030, USA

3   Department of Mechanical and Energy Engineering, Southern University of Science and Technology, No. 1088, Xueyuan Road, Shenzhen, Guangdong 518055, China

In PECM, the application of ultrashort voltage pulses with nanosecond duration enables direct 3D micromachining with a very sharp resolution. The time constant for charging the double layer on the electrodes is small enough for significant charging only at the electrode separations in the nano- to micro-meter range [11]. Since the rates of electrochemical reactions are exponentially dependent on the potential drop in the double layer, material removal is confined to these polarized electrode regions in very close proximity [12]. Wire-ECM adopts a micro-meter-scale metal wire as the tool electrode to fabricate microstructures by moving the tool electrode along a programmed toolpath. The agility of Wire-ECM makes it ideal for machining micro parts and features [13]. It is reported that microstructures with a slit width of less than 20 μm can be fabricated by a tungsten wire electrode with a diameter of 5 μm [14]. Jet-ECM refers to a fast technology for creating complex microgeometry by controlling the electric current and nozzle movement [15]. With a current density of 100 A/cm$^2$, geometries can be fabricated with excellent surface qualities [16]. Different from the aforementioned methods, TM-ECMM is considered a simple and reliable method to fabricate microcavity arrays with controlled size, location, and density. The micropatterned mask confines the workpiece dissolution to the exposed area, while current density controls the evolution of the microgroove on the workpiece surface [17–19]. Since lithography is time-consuming and labor-intensive yet essential to TM-EMM, researchers explored the feasibility of using metal oxide film as the mask [20].

In the present research, electrochemical isotropic etching is combined with thermal oxide film mask laser lithography to fabricate an array of hemispherical microcavities on different metal surfaces. The laser micropatterned the thermal oxide film on the metal surface, while the isotropic etching

through this film led to an array of well-defined hemispherical etching holes. The polarization curve and chronoamperometry were used to explore the electrochemical isotropic etching parameters, and the influence of the thermal oxide film thickness and the laser spot diameter on the etching holes was analyzed.

## Experimental approach

Commercially available pure titanium, stainless steel, pure nickel, and pure tungsten substrates with a diameter of 15 mm and thickness of 3 mm were used in this study. The substrates were lapped by SiC sandpapers (#500) to remove the rough wire-cutting marks. Then, the substrates were ultrasonically cleaned in deionized water and ethyl alcohol for 5 min to remove contaminants. During electrochemical etching, the front side of the substrate faced the cathode, while the side and back faces were covered by Teflon. Electrochemical properties were measured using an electrochemical workstation (CHI660e, Shanghai Chenhua Instrument Co., Ltd.). Before experiments, all the substrates were electropolished to remove subsurface damage. Before and after polishing, the surface morphologies were examined by scanning electron microscopy (SEM, ZEISS Merlin) and laser scanning confocal microscopy (LSCM). The surface roughness was measured by atomic force microscopy (AFM, Bruker Edge).

### Experimental setup and mechanism of isotropic etching

The schematic of the isotropic etching setup is shown in Fig. 1a. A glass beaker containing electrolytes was used as



**Fig. 1** Schematic representation of **a** the experiment setup and **b** the formation of the hemispherical hole in isotropic etching mode
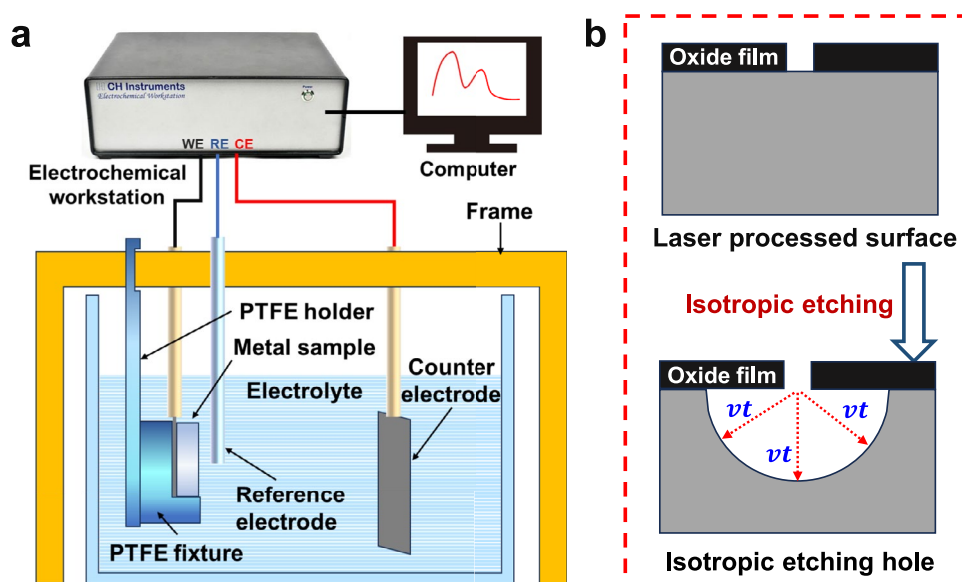
the reaction cell. The workpiece was secured by a custom fixture and connected to the working electrode of the electrochemical workstation. The counter electrode was a platinum mesh (2 cm×2 cm). A Hg/Hg$_2$SO$_4$ electrode with a standard electrode potential of 0.652 V (vs. NHE) at 298 K served as the reference electrode. The current and potential were recorded during the experiment and exported to a connected computer.

A naturally formed oxide film on the metal surface cannot be dissolved directly. The oxide film is first broken down under the influence of the electric field, followed by the matrix dissolution at the breakdown site. In isotropic etching mode, all crystal faces dissolve at the same rate, forming a hemispherical hole centered on the breakdown site on the metal surface, as shown in Fig. 1b.

According to the electricity formula:

$$Q = iAt \tag{1}$$

$$V = \frac{MQ}{nF\rho} \tag{2}$$

where $i$, $A$, $t$, $Q$, $V$, $M$, $n$, $F$, and $\rho$ are the current density, area, time, electric charge, volume, molar mass, the number of electrons in the reaction, Faraday constant, and density, respectively.

Combining Eqs. 1 and 2 in the growth rate of the etching hole radius results in the following:

$$v = \frac{V}{At} = \frac{Mi}{nF\rho} \tag{3}$$

The etched hole radius is directly proportional to the current density.

## Microfabrication process

The weak and nonuniform thickness of the natural oxide film would irregularly break down resulting in the random distribution of etching holes during direct etching. Therefore, laser ablation [21] was used to pattern the surface oxide film to locate the etching site. Additional thermal oxidation of substrates was performed to increase the oxide film thickness to ensure the etching occurs only at the laser ablation sites. For all the substrates, thermal oxidation was carried out for 1 h in a tube furnace (OFT-1200X, Hefei Kojing Material Technology Co., Ltd.). Oxidation temperatures and resulting film thicknesses for different substrates used in this study are given in Table 1. Figure 2 further describes the proposed through-mask electrochemical micromachining under isotropic etching mode involving thermal oxidation, laser dotting, and electrochemical etching.

Laser dotting of the oxide film was conducted with a picosecond laser (Grace Laser, Blazer-40F-UV) and a

**Table 1** Parameters of thermal oxidation

| Materials | TA2 | W | 304L | Ni |
|---|---|---|---|---|
| Heating temperature (°C) | 350 | 350, 400, 500 | 400, 500 | 350, 500 |
| Thickness (nm) | 20 | 25, 50, 413 | 21, 103 | 22, 141 |

femtosecond laser (Spectra Physics, SpOne-8-SHG) using a localized irradiation approach. The femtosecond laser system provided a Gaussian light spot with a 300 fs pulse width and 520-nm central wavelength. The repetition rate of laser pulses was set to 100 Hz. The laser beam was focused by a 0.1 NA, 4X objective with a beam waist radius of 2.56 μm, resulting in a laser fluence of 1.4 J/cm$^2$. The radius was determined from a laser ablation test [19]. A high-precision moving stage with a step resolution of 10 nm on both the x- and y-axes controlled the sample movement. The scanning speeds and intervals were set to 4 mm/s and 40 μm, respectively. The picosecond laser had a pulse width of 10 ps and a wavelength of 350 nm. The laser beam was controlled using a galvanometer scanner (SCANLAB, Germany) equipped with an F-theta lens with a focal length of 163 mm. The
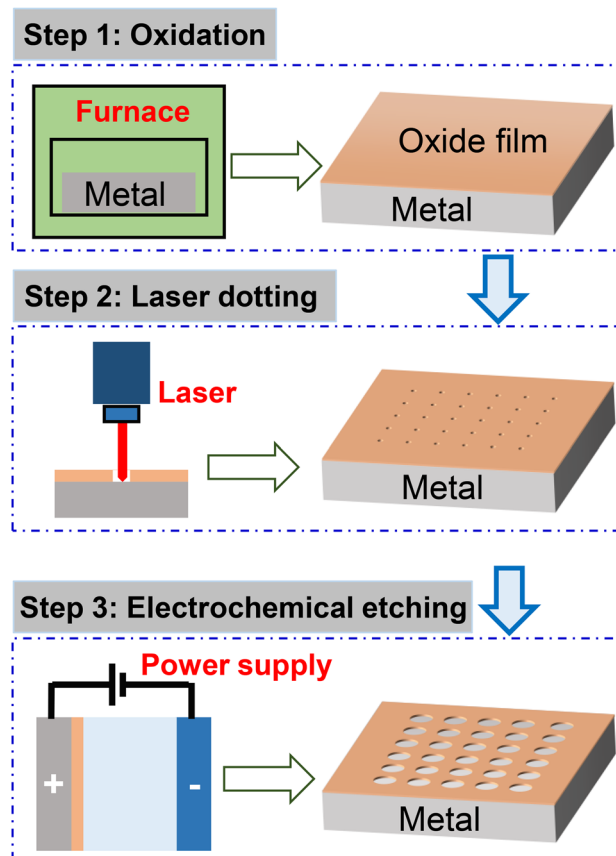


**Fig. 2** Schematics of thermal oxidation, laser dotting, and electrochemical etching

diameter of the focused spot was ca. 15 μm. The repetition frequency was set to 10 kHz, resulting in a laser fluence of 0.57 J/cm$^2$. Since the oxide film is nanometer-scale, both picosecond and nanosecond laser dotting use a single pulse. Further details on laser dotting parameters are given in Table 2.

The electrochemical etching, as described in Fig. 1a, was carried out at room temperature in an electrolyte containing analytical-grade sulfuric acid (97%) and methanol (99.5%). The etching parameters used in this study are shown in Table 3.

## Results and discussion

### Anodic dissolution behavior of pure titanium

As a preliminary investigation, the polarization curve of pure titanium (TA2) was measured in the electrolyte with a 1:100 volume ratio of $H_2SO_4$ to $CH_3OH$, as shown in Fig. 3a. $CH_3OH$ acts as an efficient destabilizing agent of the surface oxide films [22]. The anodic polarization curve is divided into three regions. In region i, the current density increased with the increasing potential (−0.7 V to −0.6 V), where the overpotential provides the activation energy to drive the dissolution process [23]. Therefore, the crystal surface dissolution rate varies with crystal orientation because of the activation energies varying with the crystal planes. The current density hardly changed with the potential (−0.6 V to 0 V) in region ii, indicating mass transfer polarization during titanium dissolution. In this region, the metal dissolution rate did not increase with potential due to the accumulation of reaction products on the surface. However, a further increase in the potential from 0 to 10 V increased the current density, indicating unstable mass transfer polarization in region iii.

Figure 3b shows the TA2 polarization curve in an electrolyte with a 10:100 volume ratio of $H_2SO_4$ to $CH_3OH$. Again, the anodic polarization curve was divided into three regions. The current density increased with the potential

**Table 3** Electrochemical etching parameters

| Materials | TA2 | W | 304L | Ni |
|---|---|---|---|---|
| Electrolytes composition ($V_{sulfuric\ acid}/V_{methanol}$) | $\frac{1}{100}$, $\frac{10}{100}$ | $\frac{15}{100}$ | $\frac{10}{100}$ | $\frac{20}{100}$ |
| Etching potential (V) | 2 | 5 | 5 | 5 |
| Electrolyte temperature (°C) | 25 | 25 | 25 | 25 |

(−0.4 V to 0.4 V) in the region i corresponding to the activation polarization in this range. The current density hardly changed with the applied potential (0.4 to 9.5 V) in region ii, indicating mass transfer polarization of TA2 dissolution. The polarization curve of tungsten in the electrolyte with a 15:100 volume ratio of $H_2SO_4$ to $CH_3OH$ also demonstrated a similar trend [24]. However, the current density increased with the potential beyond 9.5 V (region iii), possibly due to side reactions. Typically anodic dissolution under the mass
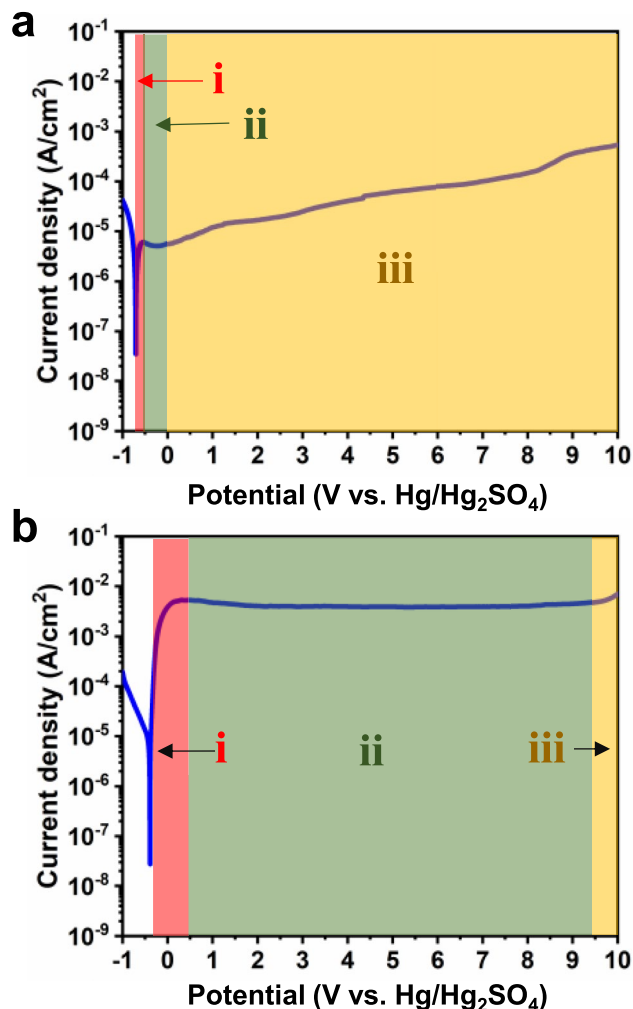
**Fig. 3** Polarization curves of TA2 in electrolytes with **a** 1:100 and **b** 10:100 volume ratios of $H_2SO_4$ to $CH_3OH$

**Table 2** Laser dotting parameters

| Parameters | Picosecond laser | Femtosecond laser |
|---|---|---|
| Model | Grace Laser Blazer-40F-UV | Spectra Physics SpOne-8-SHG |
| Pulse width | 10 ps | 300 fs |
| Central wavelength | 350 nm | 520 nm |
| Repetition rate | 100 kHz | 100 Hz |
| Laser fluence | 0.57 J/cm$^2$ | 1.4 J/cm$^2$ |
| Focused spot diameter | 15 μm | 5.12 μm |
| Distance between the centers of the holes | 50 μm | 40 μm |

transport limitation governs the electropolishing process [25]. An electrolyte with a 10:100 volume ratio of $H_2SO_4$ to $CH_3OH$ is suitable for the isotropic etching of TA2 due to the stable mass transfer polarization region observed in the polarization curve.

Chronoamperometry was performed to study the surface morphology evolution of TA2 in the activation and mass transfer polarization regions. Figure 4a shows the current density-time curves at −0.5 V and 2 V in an electrolyte with a 1:100 volume ratio of $H_2SO_4$ to $CH_3OH$. The current density at −0.5 V, within the activation polarization region, remained constant due to the rapid transfer of reactive products and negligible mass transfer effects. The current density at 2 V initially increased slightly before reaching a plateau. As seen from Fig. 3a, the TA2 dissolution enters mass transfer polarization at −0.6 V, which became unstable when the potential is raised above 0 V. Therefore, the current
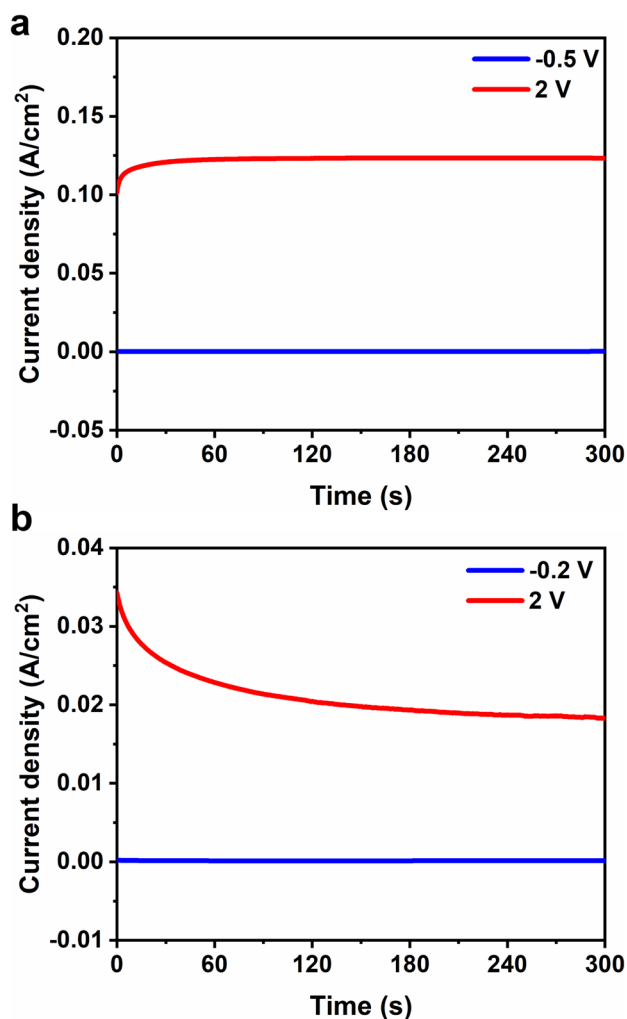
density-time curve did not show a decreasing trend in the early stage when the potential was 2 V.

Figure 4b shows the current density-time curves obtained at −0.2 V and 2 V in an electrolyte with a 10:100 volume ratio of $H_2SO_4$ to $CH_3OH$. The current density at −0.2 V remained almost unchanged because of the activation polarization where no mass transfer occurs. The curve obtained at a potential of 2 V decreased sharply in the beginning and then reached a plateau. According to the polarization curve in Fig. 2b, 2 V is in the range of the mass transfer polarization region, so the current density-time curve decreased due to the etching products accumulation. The steep decrease in the current is due to the balance of ion diffusion and metal dissolution during the electropolishing of tungsten [26].

The TA2 surface was etched for 5 min in an electrolyte with a 1:100 volume ratio of $H_2SO_4$ to $CH_3OH$ at −0.5 V. An irregularly shaped etching hole (see Fig. 5a) with a rough inner surface (see Fig. 5b) was formed on TA2. The anisotropic etching and rough inner surface emerged due to the active polarization. The microcavities were formed due to the protective passivation film on the surface [27]. The spontaneously formed passivation film on TA2 was 10-nm thick, as measured by an ellipsometer (Film Sense FS-1). The passivation film protected the underlying metal matrix from the electrolyte, while the dissolution occurred only at the passivation layer breakdown sites, resulting in the formation of microcavities. Similar microcavities have been reported on titanium surfaces with highly active halogen salts in the electrolyte [28, 29]. Besides, TA2 etching at 2 V for 1 min formed hemispherical microcavities on the surface, while a residual passivation film was observed at the edge of the hole, as shown in Fig. 5c. As evident from Fig. 3a, 2 V is within the mass transfer polarization region that resulted in the isotropic etching of the TA2 surface.

In contrast, 5 min etching at 2 V produced irregular microcavities on the surface, as shown in Fig. 5d. The microcavity formed on the TA2 surface was similar to that of the hexagonal-close-packed (hcp) structure. The formation of irregular microcavities indicated the TA2 dissolution in the active polarization region because the applied potential was in the unstable mass transfer polarization region. The anisotropic etching of aluminum is useful in various functional devices requiring a large surface area, such as substrates for catalysts and electrodes for electrolytic capacitors [30].

The TA2 surface was etched for 5 min in an electrolyte with a 10:100 volume ratio of $H_2SO_4$ to $CH_3OH$ at −0.2 V. An irregularly shaped etching hole (see Fig. 6a) with a rough inner surface (see Fig. 6b) was observed, likely due to −0.2 V being in the activation polarization region that resulted in the anisotropic dissolution of TA2. In addition, the step-like structures at the inner surface are indicative of crystallographic etching. The electrochemical dissolution of tungsten in a 2 wt.% electrolyte produced similar etching
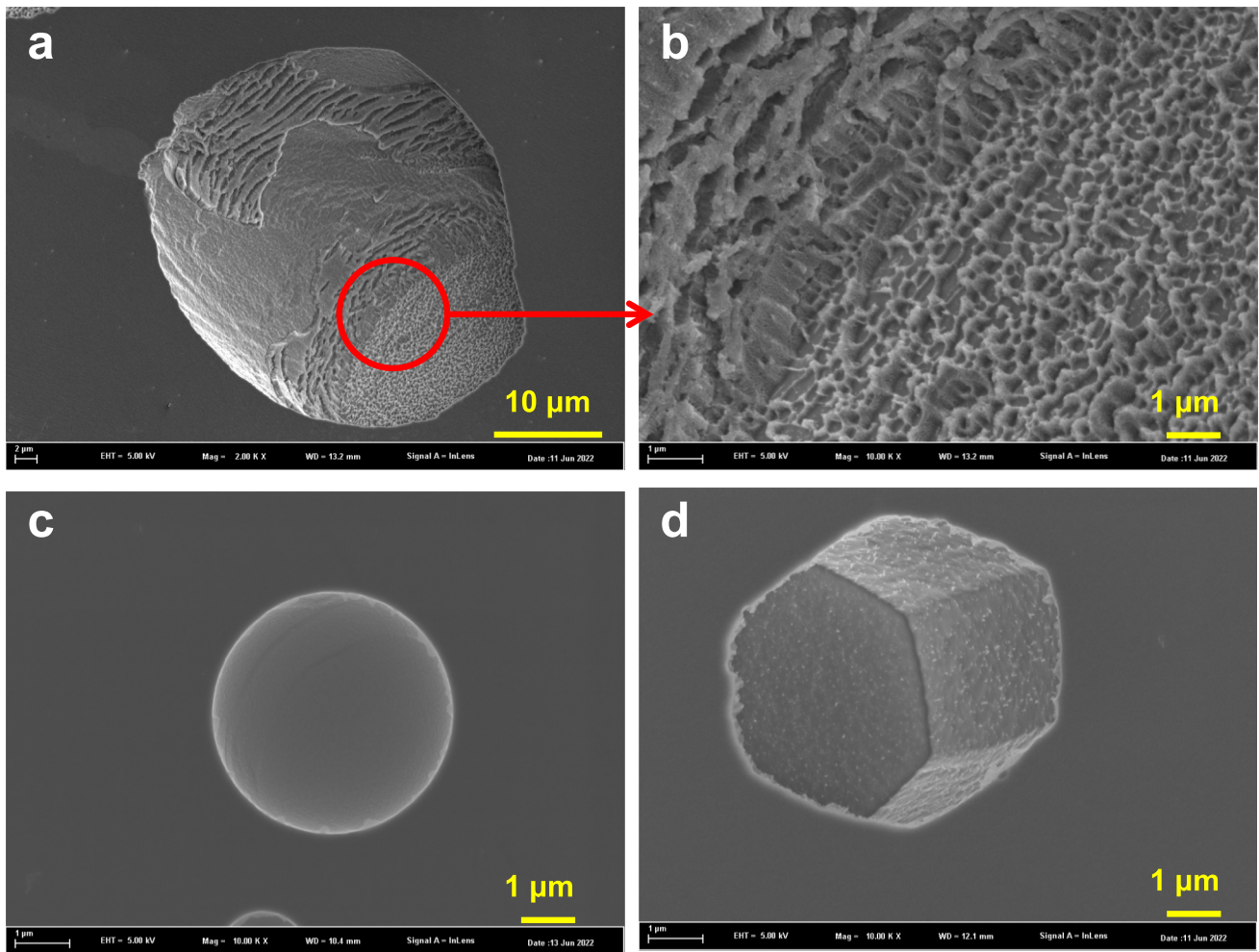


**Fig. 4** Chronoamperometry plots obtained at different potentials in electrolytes with **a** 1:100 and **b** 10:100 volume ratios of $H_2SO_4$ to $CH_3OH$
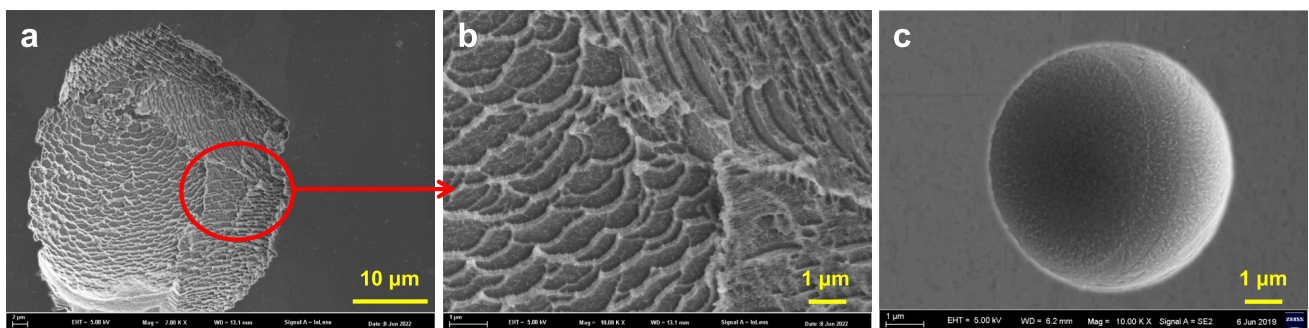
**Fig. 5** Surface morphology of TA2 after etching in the electrolyte with a 1:100 vol ratio of $H_2SO_4$ to $CH_3OH$: **a, b** 5 min under a potential of -0.5 V (vs. $Hg/Hg_2SO_4$); **c** 1 min and **d** 5 min under a potential of 2 V (vs. $Hg/Hg_2SO_4$)

marks on some grains [31]. Besides, etching at 5 V for 5 min formed hemispherical microcavities on the TA2 surface, as shown in Fig. 6c. According to the polarization curve in Fig. 3b, the applied potential (2 V) being in the mass transfer polarization region ensured the isotropic dissolution of TA2. In the early stage of electrochemical machining of TB6 titanium alloy, local corrosion on the anode surface produced hemispherical etching holes [32].



**Fig. 6** Surface morphology of TA2 after etching in the electrolyte with a 10:100 vol ratio of $H_2SO_4$ to $CH_3OH$: **a, b** 5 min under a potential of −0.2 V (vs. $Hg/Hg_2SO_4$); **c** 5 min under a potential of 2 V (vs. $Hg/Hg_2SO_4$)

## Array structure on TA2

For TA2, there is a natural tendency of approximately 10-nm-thick passivation layer formation. However, this passivation layer is relatively weak and microcavities can be formed even at 2 V as explained in the previous section. Therefore, TA2 was thermally oxidized to generate a thick oxide film as a mask to ensure that subsequent electrochemical dissolution occurred only where the oxide film was removed. The oxide film thickness depends on the temperature/time parameters [33]. For example, the oxide layers obtained at 600 °C had thicknesses ranging from 0.40 to 1.37 μm when thermally oxidized for 6 to 72 h, respectively. In this research, TA2 was thermally oxidized at 350 °C to achieve a 20-nm film thickness as measured by ellipsometry.

As shown in Fig. 7a, an array of microcavities was formed on the thermally oxidized TA2 surface with the picosecond laser beam. The interval of the laser beam dotting was 50 μm. The surface oxidation of titanium can result in different colors [34], so when the oxide film at the laser processing site was removed, its color was different from the surrounding oxide film. Laser processing exposed approximately 20-μm diameter circular areas on the substrate. Figure 7b shows the profile of a hole from Fig. 7a. As the laser energy was exceedingly low and each dot was only machined by a single pulse, the oxide film was entirely removed with minimal substrate removal. Therefore, the profile is close to a straight line.

After laser dotting, TA2 was electrochemically etched at 2 V for 1 min. As shown in Fig. 7c, an array of microcavities was formed on the TA2 surface. The dissolution of the substrate occurred only where the oxide film was removed, indicating that the thickness of the thermal oxide film was sufficient to protect the substrate from etching. As the applied potential (2 V) was in the mass transfer polarization region, the inner surface was smooth and shiny. Figure 7d shows the horizontal and vertical profiles of a microcavity from Fig. 7c. The depth of the microcavity was 11.0 μm, and the horizontal and vertical widths were 36.5 μm and 34.0 μm, respectively, slightly deviating from hemispherical shape. The electrochemical dissolution initiated from unmasked regions and then spread inward at the same speed. Therefore, the relatively large diameter of the laser-processed area resulted in a relatively smaller depth and deviation in the shape of the etching microcavity. At the beginning of dissolution, the maximum etch rate occurs near the photoresist mask [35] and proceeds toward the center as the etching progresses. The pattern in the resist must be at least three times smaller than the final opening diameter to obtain hemispherical cavities [36]. Therefore, to obtain a hemispherical array of cavities, a feasible method is to reduce the area where the oxide film is removed by the laser. Hemispherical microcavities can be formed on pure titanium with a breakdown site diameter of the oxide film of approximately 2 μm [37]. A femtosecond laser was used in the following section to obtain a smaller laser machining area.

A femtosecond laser beam formed an array of microcavities on a thermally oxidized TA2 surface, as shown in Fig. 8a. The laser-processed regions were brighter than the oxide film due to the exposure of the metal matrix. The



**Fig. 7** Morphology and cross-sectional profile of the microcavities measured by LSCM: **a**, **b** after picosecond laser dotting; **c**, **d** after etching in an electrolyte with a 10:100 volume ratio of $H_2SO_4$ to $CH_3OH$
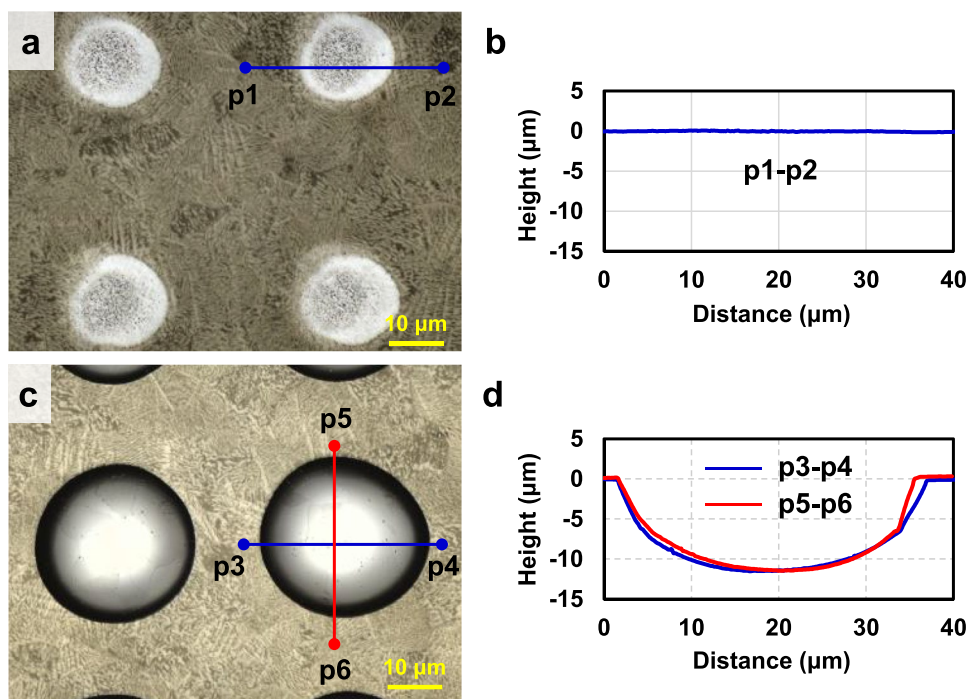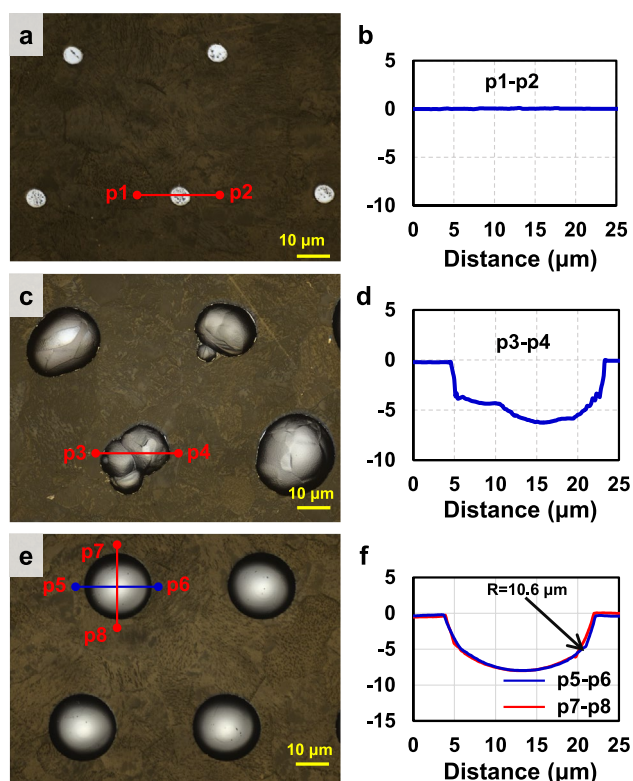
**Fig. 8** Morphology and cross-sectional profile of the microcavity measured by LSCM: **a**, **b** femtosecond laser dotting; **c**, **d** after etching in the electrolyte with a 1:100 vol ratio of $H_2SO_4$ to $CH_3OH$; **e**, **f** after etching in the electrolyte with a 10:100 vol ratio of $H_2SO_4$ to $CH_3OH$

exposed area was approximately circular, with a diameter of approximately 5 μm. The profile of a microcavity from Fig. 8a is shown in Fig. 8b. As the material removal was small, the profile was also close to a straight line. Figure 8c shows the microcavities on the surface after electrochemical dissolution in an electrolyte with a 1:100 volume ratio of $H_2SO_4$ to $CH_3OH$ at 2 V for 1 min. The etching cavities varied in shape due to the applied potential being in the unstable mass transfer polarization region, as demonstrated previously. The non-hemispherical profile of a microcavity is shown in Fig. 8d. Irregularly shaped cavities with rough surfaces were also reported on dissolving titanium in NaBr electrolyte at 5 V [38]. Figure 8e shows microcavities formed on the TA2 surface after electrochemical dissolution in the electrolyte with a 10:100 volume ratio of $H_2SO_4$ to $CH_3OH$ at 2 V for 1 min. From the top view, these etching holes appeared to be hemispherical. As shown in Fig. 8f, the horizontal and vertical profiles of a microcavity in Fig. 8e were semicircular with a 10.6 μm identical radius. Microcavities with a diameter of 40 μm were reported on titanium after anodic dissolution for 23 min in 3 M $H_2SO_4$ in $CH_3OH$ electrolyte [39]. These experiments demonstrate that the small oxide film removal area and suitable electrochemical

parameters are important to ensure dissolution in a stable mass transfer polarization region for the formation of hemispherical microcavities. Surface topography is an important surface property and affects the biological performance of titanium implants [40]. Therefore, the preparation of well-defined microstructure arrays on the surface is beneficial to the medical applications of titanium alloys.

Figure 9a shows that the radius of the microcavities increases linearly with time when other parameters such as applied potential and the dissolution rate are constant. Figure 9b and c shows the microcavities formed on the titanium surface after etching for 1 min and 3 min, respectively. The microcavities had a regular hemispherical shape (see Fig. 9b), which showed 40 μm diameter and deviated from the hemispherical shape (see Fig. 9c). Additionally, small etching holes are observed around the microcavities, indicating that the oxide film was broken down in the long-term etching process. Therefore, to obtain large-scale and regular-shaped microcavities, the performance of the oxide film needs to be further enhanced.

## Array structure on other metals

Surface structuring by combining thermal oxide film laser lithography and isotropic etching has also been applied to other metals, such as stainless steel, pure nickel, and tungsten. As a preliminary investigation, the polarization curves of stainless steel, pure nickel, and tungsten were measured as shown in Fig. 10.

Figure 10a shows the polarization curve of stainless steel in the electrolyte with a 10:100 volume ratio of $H_2SO_4$ to $CH_3OH$. In the potential range from 2.5 to 10 V, the current density hardly changed with the potential, demonstrating that the dissolution of the stainless stain was mass transfer polarization [41]. Figure 10b shows the polarization curve of pure nickel in the electrolyte with a 20:100 volume ratio of $H_2SO_4$ to $CH_3OH$. It can be inferred that the mass transfer polarization region was 1.5 to 10 V [42]. Figure 10c shows the polarization curve of tungsten in the electrolyte with a 15:100 volume ratio of $H_2SO_4$ to $CH_3OH$, and the mass transfer polarization region was 3.5 to 10 V.

The electropolishing can be obtained in the current density plateau region [43]. Obviously, for stainless steel, pure nickel, and tungsten, a stable mass transfer polarization region existed in the polarization curve when suitable electrolytes were used. Therefore, in the subsequent electrochemical dissolution experiments, the applied potential is selected based on the polarization curve.

To obtain a controllable array structure on the metal surface, the first step is to form an oxide film on the metal surface. Since a 20-nm-thick oxide film was sufficient to protect the matrix from etching. Therefore, the stainless steel, pure nickel, and tungsten were also thermally oxidized to achieve a
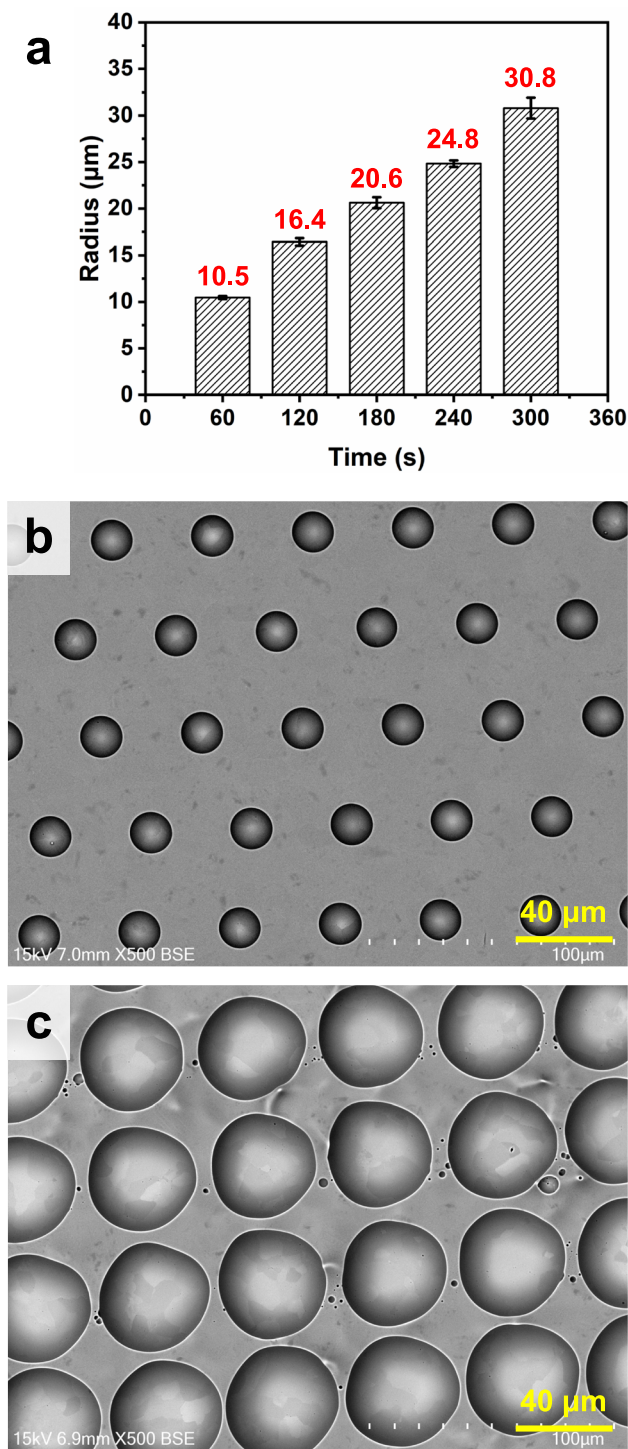
**Fig. 9** **a** The radius of the microcavities with etching time. **b** Array microcavities on titanium after etching for 1 min. **c** Array microcavities on titanium after etching for 3 min
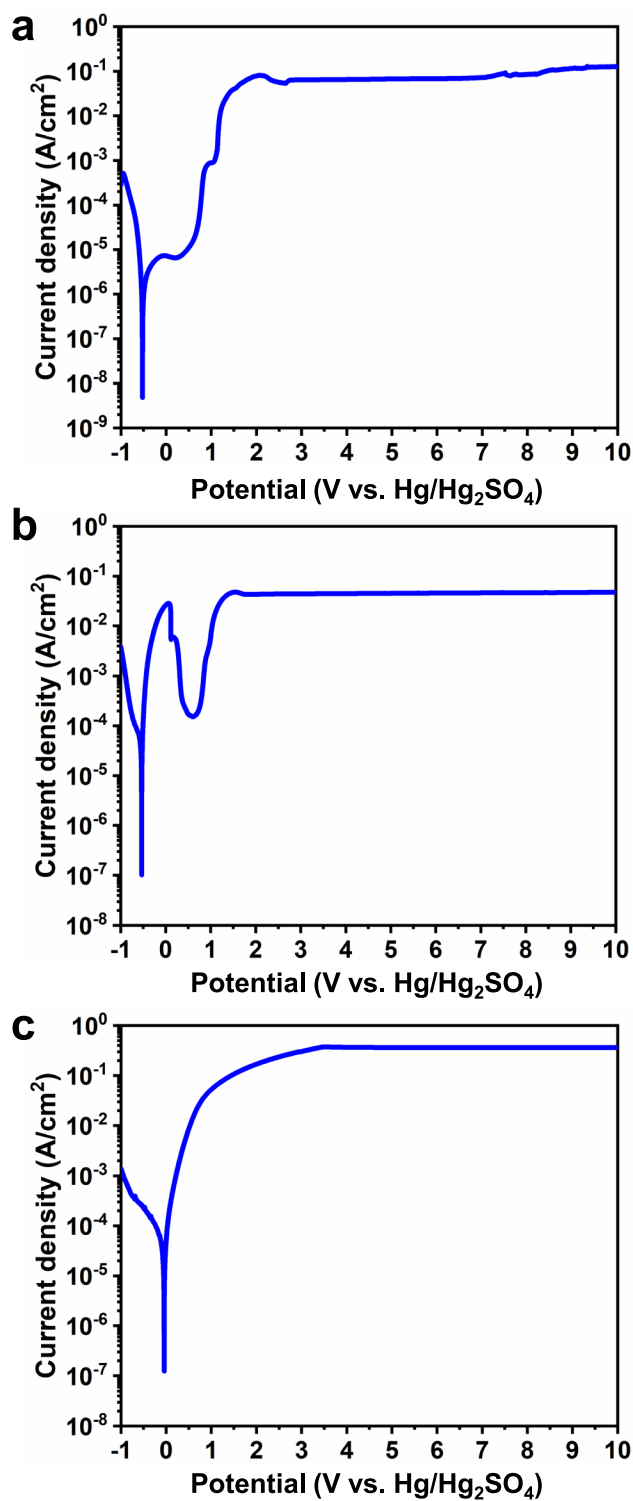


**Fig. 10** Polarization curves of **a** stainless steel, **b** pure nickel, and **c** tungsten in electrolytes with different volume ratios of $H_2SO_4$ to $CH_3OH$

similar thickness. Thermal oxidation of stainless steel at 400 °C for an hour developed a 21-nm-thick oxidation film. The pure nickel and tungsten were oxidized at 350 °C for an hour, and the oxide film thicknesses were 22 nm and 25 nm, respectively.

According to the polarization curve in Fig. 10, when the applied potential is greater than 2.5 V, 1.5 V, and 3.5 V, the dissolution of stainless steel, nickel, and tungsten,

respectively, enters the mass transfer polarization region. Therefore, 5 V was chosen as the applied potential for electrochemical dissolution experiments for stainless steel, nickel, and tungsten.

The morphology of the stainless steel after electrochemical dissolution is shown in Fig. 11a. The entire stainless steel surface was dissolved, and distinguishing the laser processing site was difficult, indicating that the oxide film could not protect the substrate. The morphology of the pure nickel after electrochemical dissolution is shown in Fig. 11b. Preferential dissolution occurred at the laser processing site. Still, dissolution at other areas indicated weak protection by the oxide film. Similarly, the dissolution of tungsten also occurred on the whole surface, as shown in Fig. 11c. Therefore, approximately 20-nm-thick oxide film is not sufficient to avoid the dissolution of stainless steel, pure nickel, and tungsten substrates.

Once again, stainless steel, pure nickel, and tungsten were thermally oxidized at 500 °C for an hour, resulting in the formation of oxide films with thicknesses of 103 nm, 141 nm, and 413 nm, respectively. Despite the 103-nm-thick passivation film, the electrochemical dissolution occurred on the entire surface of stainless steel, as shown in Fig. 11d. As shown in Fig. 11e, upon increasing the oxide film thickness to 141 nm, cracks were observed on the pure nickel surface, with tiny holes forming around the microcavity. Therefore a thicker oxide film could not protect stainless steel and pure nickel from electrochemical dissolution.

In contrast, the electrochemical dissolution of tungsten with 413-nm-thick oxide film occurred only at the laser-machined sites, as shown in Fig. 11f. Raised oxides were randomly distributed on the surface and formed during thermal oxidization. These raised oxides deteriorated the surface quality and reduced the uniformity of laser machining. In conclusion, among stainless steel, pure nickel, and tungsten, the oxide film can only mask tungsten and facilitate microstructural array fabrication. However, low thermal oxidation temperatures can produce more uniform oxide film on the surface. Therefore, the thermal oxidation temperature for tungsten was reduced to 400 °C for the following experiments.

At a potential larger than 3.5 V, the dissolution of tungsten was mass transfer polarization, as seen in Fig. 10c. The current density-time curves for tungsten obtained at 2 V and 5 V are shown in Fig. 12a. The tungsten was thermally oxidized at 400 °C for 1 h, achieving approximately 50-nm-thick oxide film. As 2 V is in the active polarization region, the current density does not change significantly. Besides, 5 V is in the mass transfer polarization region, and the initial decreasing tendency of the current density over time is due to the accumulating etching products. As the etching duration increases, the current density increases regardless of the applied potential, which is due to the growing reaction area of microcavities.

The surface morphologies after electrochemical dissolution for 5 min at 2 V and 5 V are shown in Fig. 12b and c, respectively. At 2 V, which is in the activation polarization
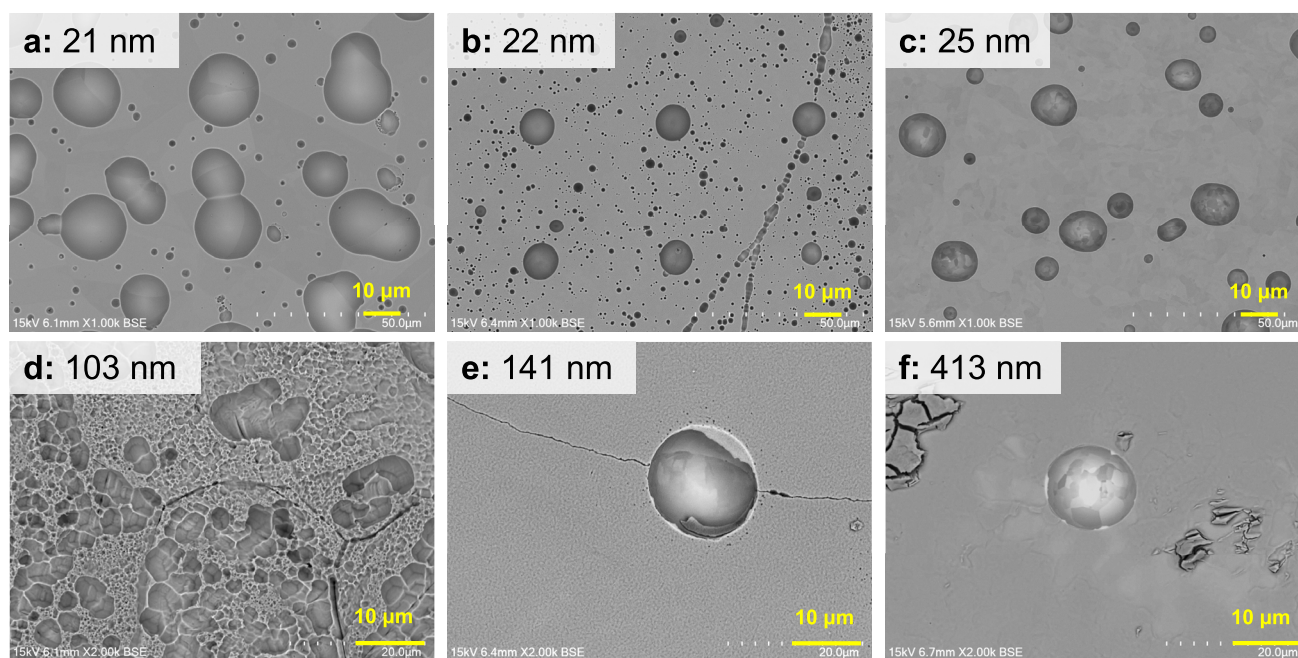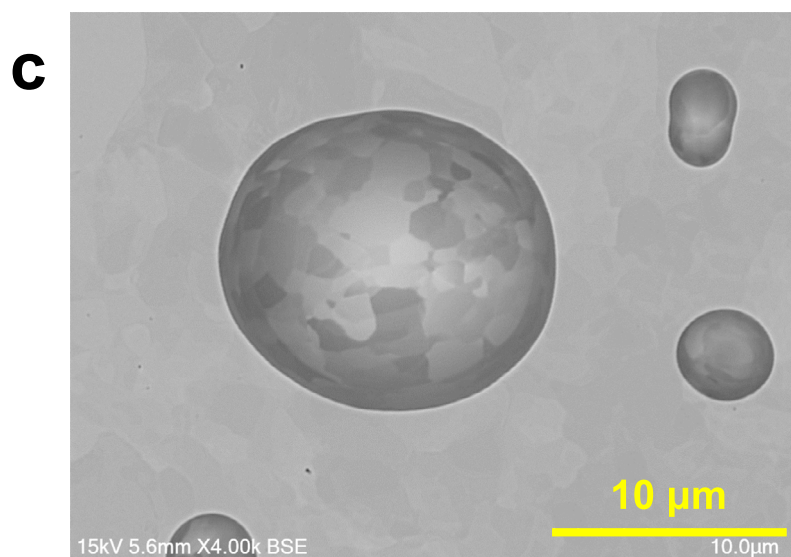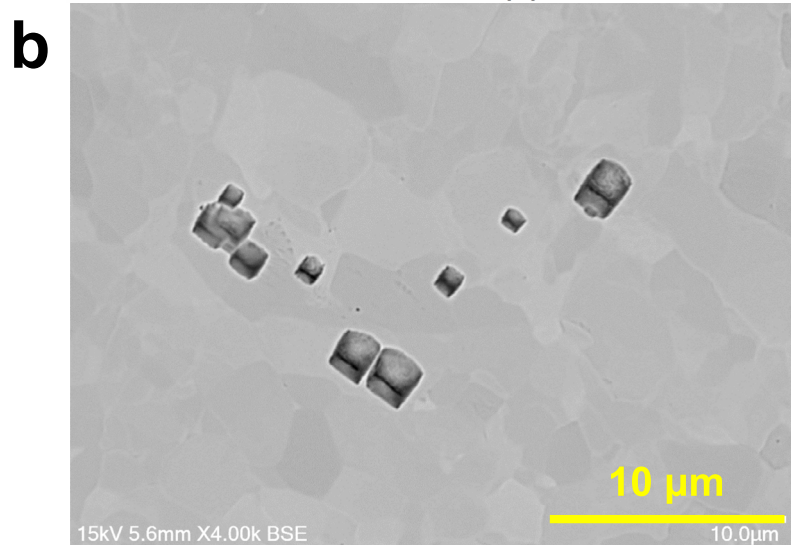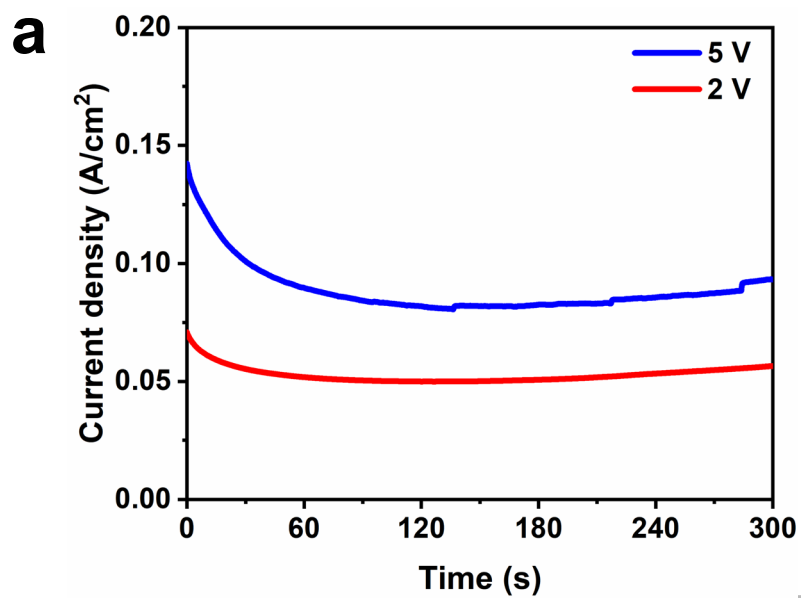


**Fig. 11** Morphology of array microcavities formed on stainless steel (**a**, **d**), pure nickel (**b**, **e**), and tungsten (**c**, **f**)

**Fig. 12** **a** Chronoamperometry plots of tungsten obtained at different potentials in an electrolyte with a 15:100 vol ratio of $H_2SO_4$ to $CH_3OH$. Surface morphology after etching for 5 min under potentials of **b** 2 V (vs. $Hg/Hg_2SO_4$) and **c** 5 V (vs. $Hg/Hg_2SO_4$)

region, the dissolution rate varies with the crystal planes, resulting in irregular microcavities. As shown in Fig. 12c, etching at 5 V for 5 min formed approximately hemispherical with smooth such that the crystalline grains with different orientations can be distinguished. Therefore, 5 V is reasonable to fabricate array structures on a tungsten surface.

An array of hemispherical microcavities formed on the thermally oxidized tungsten surface after electrochemical etching at 5 V for 1 min is shown in Fig. 13. The distance between adjacent microcavities is 40 μm. The crystalline grains with different orientations can be distinguished on the inner surface of a microcavity shown in Fig. 13b. Figure 13c shows the semicircular profiles of three adjacent microcavities from Fig. 13a. The radii of the three microcavities are 6.77 μm, 6.82 μm, and 6.74 μm, indicating uniform growth of these microcavities. The surface roughness of tungsten after oxidation was 3.14 nm, as shown in Fig. 13d, which reduced to 2.02 nm for the inner surface of the cavity after electrochemical dissolution in the mass transfer polarization region, as shown in Fig. 13e. The microlens arrays exhibit good optical properties, such as an extremely large field of view angle [44]. Fabricating the array structure on tungsten makes it possible to process microlenses using tungsten as a mold.

The microcavity radii grow linearly with the etching time, as shown in Fig. 14a. However, as the radius of the microcavities increased to approximately 40 μm, small microcavities formed on the whole surface, indicating that the oxide film was broken down during the etching process. This shows that the performance of the oxide film is very important for the preparation of definite array microcavities.



**Fig. 13** Morphology and cross-sectional profile of the microcavities measured by **a**, **b** SEM and **c** LSCM. Surface roughness measured by AFM: **d** oxide film and **e** inner surface of a microcavity
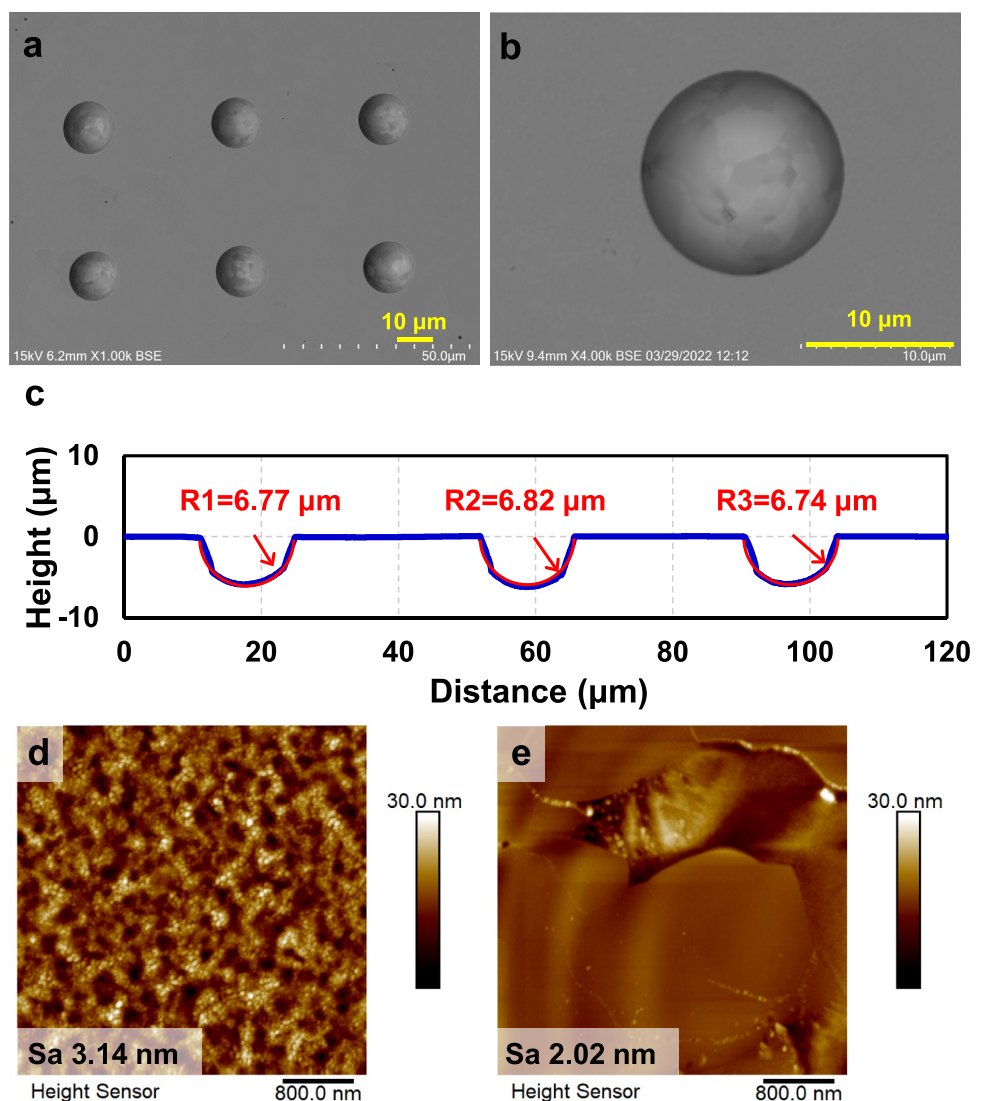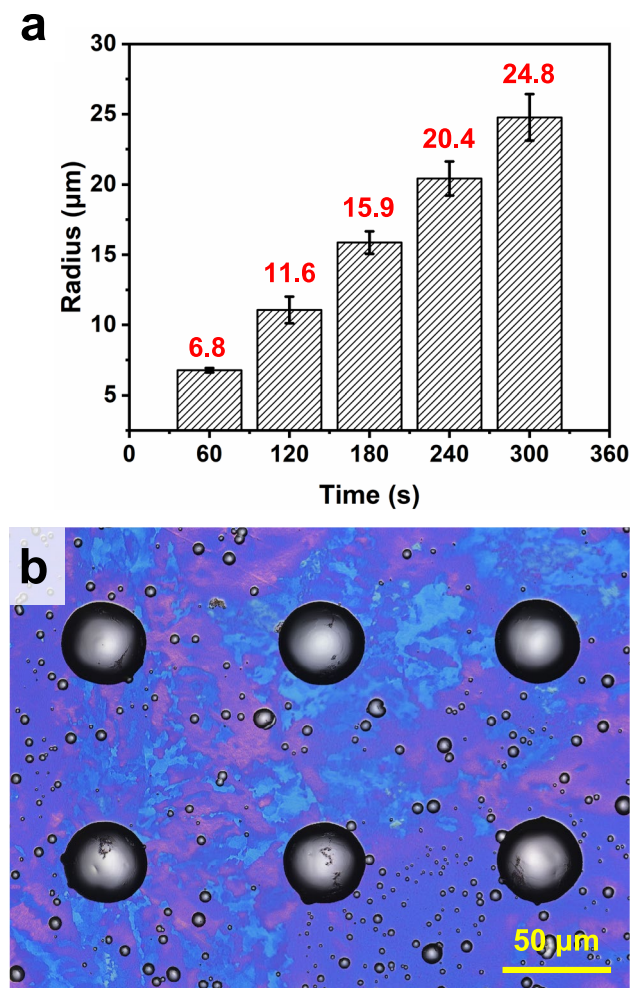
**Fig. 14** Variation in the diameter of array microcavities for different etching times (**a**) and array microcavities after etching for 4 min (**b**)

## Conclusions

In this paper, surface structuring through thermal oxide film mask laser lithography and electrochemical isotropic etching was investigated, and an array of hemispherical microcavities was generated on different metal surfaces. To summarize, the following conclusions can be drawn from this study:

- The oxide film formed by thermal oxidation acts as a mask in this study. Thermal oxidation of TA2 and tungsten at 350 °C and 400 °C produced 20 nm and 50-nm-thick oxidation films, respectively, which were sufficient to avoid their electrochemical dissolution. However, even more than 100-nm-thick oxide films on stainless steel and pure nickel could not mask their electrochemical dissolution.

- In the laser ablation experiment, picosecond and femtosecond lasers produced nearly circular ablation shapes on TA2 with 15 µm and 5 µm diameters, respectively. However, after etching for 1 min, the surface processed by the picosecond laser exhibited a larger size and deviated from a hemispherical shape, indicating that femtosecond laser processing has higher stability.

- Surface structuring through laser lithography and electrochemical isotropic etching generated an array of hemispherical microcavities on TA2, achieving a 10.6 µm radius after etching at 2 V for 1 min.

- A highly stable and protective oxide film is needed to achieve a controllable hemispherical microcavity array on metal. The film produced on tungsten was more stable compared to SUS304 and nickel allowing microstruring of tungsten only. The electrochemical etching of tungsten at 5 V for 1 min formed hemispherical microcavities of approximately 6.8 µm radius.

## Declarations

**Competing interests** The authors declare no competing interests.

## References

1. Wu B, Yan D, Lin J, Song J (2023) Wire electrochemical etching of superhydrophobic nickel surfaces with enhanced corrosion protection. Materials 16:7472
2. Yan D, Chen Y, Liu J, Song J (2023) Super-fast fog collector based on self-driven jet of mini fog droplets. Small 19:2301745
3. Wu S, Yan D, Chen Y, Song J (2024) Self-driven oil/water separator with super-high separation rate. Nano Energy 119:109066
4. Zwahr C, Voisiat B, Welle A, Günther D, Lasagni AF (2018) One-step fabrication of pillar and crater-like structures on titanium using direct laser interference patterning. Adv Eng Mater 20:1800160
5. Sun A, Chang Y, Liu H (2018) Metal micro-hole formation without recast layer by laser machining and electrochemical machining. Optik 171:694–705
6. Leese RJ, Ivanov A (2016) Electrochemical micromachining: an introduction. Adv Mech Eng 8(1):1687814015626860
7. Landolt D, Chauvy PF, Zinger O (2003) Electrochemical micromachining, polishing and surface structuring of metals: fundamental aspects and new developments. Electrochim Acta 48:3185–3201
8. Schuster R, Kirchner VV, Allongue P, Ertl G (2000) Electrochemical micromachining. Science 289:98–101
9. Kumar A, Das M (2021) Multiphysics simulation and experimental investigation of microtool fabricated by EMM. Mater Manuf Processes 36:1489–1500

10. Patel DS, Sharma V, Jain VK, Ramkumar J (2020) Reducing over-cut in electrochemical micromachining process by altering the energy of voltage pulse using sinusoidal and triangular waveform. Int J Mach Tools Manuf 151:103526

11. Spieser A, Ivanov A (2013) Recent developments and research challenges in electrochemical micromachining (μECM). Int J Adv Manuf Technol 69:563–581

12. Cagnon L, Kirchner V, Kock M, Schuster R, Ertl G, Gmelin WT, Kück H (2003) Electrochemical micromachining of stainless steel by ultrashort voltage pulses. Z Phys Chem 217:299–314

13. Sharma V, Patel DS, Jain VK, Ramkumar J (2020) Wire electrochemical micromachining: an overview. Int J Mach Tools Manuf 155:103579

14. Zhu D, Wang K, Qu NS (2007) Micro wire electrochemical cutting by using in situ fabricated wire electrode. CIRP Ann 56:241–244

15. Hackert-Oschätzchen M, Meichsner G, Zinecker M, Martin A, Schubert A (2012) Micro machining with continuous electrolytic free jet. Precis Eng 36:612–619

16. Natsu W, Ikeda T, Kunieda M (2007) Generating complicated surface with electrolyte jet machining. Precis Eng 31:33–39

17. Sun Y, Ling S, Zhao D, Liu J, Liu Z, Song J (2020) Through-mask electrochemical micromachining of micro pillar arrays on aluminum. Surf Coat Technol 401:126277

18. Singh Patel D, Agrawal V, Ramkumar J, Jain VK, Singh G (2020) Micro-texturing on free-form surfaces using flexible-electrode through-mask electrochemical micromachining. J Mater Process Technol 282:116644

19. Wang GQ, Zhu D, Li HS (2018) Fabrication of semi-circular micro-groove on titanium alloy surface by through-mask electrochemical micromachining. J Mater Process Technol 258:22–28

20. Chauvy PF, Hoffmann P, Landolt D (2001) Electrochemical micromachining of titanium through a laser patterned oxide film. Electrochem Solid State Lett 4(5):C31

21. Zhang J, Chen Y, Zhang Y, Wu S, Sun J, Liu X, Song J (2024) Fabrication and energy collection of superhydrophobic ultra-stretchable film. Adv Funct Mater 34(27):2400024

22. Reggiani RC, Mazza F, Sivieri E (1979) Electrochemical polishing of titanium in perchloric-methanolic solutions. Mater Chem 4:149–158

23. Bard A, Faulkner L (2002) Electrochemical methods: fundamentals and applications

24. Yi R, Ji J, Zhan Z, Deng H (2022) Mechanism study of electropolishing from the perspective of etching isotropy. J Mater Process Technol 305:117599

25. Han W, Fang F (2019) Fundamental aspects and recent developments in electropolishing. Int J Mach Tools Manuf 139:1–23

26. Wang F, Zhang X, Deng H (2019) A comprehensive study on electrochemical polishing of tungsten. Appl Surf Sci 475:587–597

27. Macdonald DD, Urquidi-Macdonald M (1990) Theory of steady-state passive films. J Electrochem Soc 137:2395

28. Ittah R, Amsellem E, Itzhak D (2014) Pitting corrosion evaluation of titanium in NH4Br solutions by electrochemical methods. Int J Electrochem Sci 9:633–643

29. He Y, Lu W, Gan W, Zhao J, Zuo D (2016) Polarization of Ti6Al4V alloy in NaBr electrolyte and surface fractal analysis. Proc Inst Mech Eng Part L J Mater Design Appl 232:602–609

30. Yanagishita T, Imaizumi M, Kondo T, Masuda H (2017) Formation of porous Al particles by anisotropic anodic etching. Electrochem Commun 78:26–28

31. Chen P, Chen Y, Lin H, Li H, Li X (2021) An efficient electrochemical polishing of tungsten with combined forced and natural convections. Int J Adv Manuf Technol 117:2819–2834

32. Liu W, Ao S, Li Y, Liu Z, Zhang H, Manladan SM, Luo Z, Wang Z (2017) Effect of anodic behavior on electrochemical machining of TB6 titanium alloy. Electrochim Acta 233:190–200

33. Aniołek K (2017) The influence of thermal oxidation parameters on the growth of oxide layers on titanium. Vacuum 144:94–100

34. Pérez del Pino A, Fernández-Pradas JM, Serra P, Morenza JL (2004) Coloring of titanium through laser oxidation: comparative study with anodizing. Surf Coat Technol 187:106–112

35. Madore C, Piotrowski O, Landolt D (1999) Through-mask electrochemical micromachining of titanium. J Electrochem Soc 146:2526–2532

36. Zinger O, Chauvy PF, Landolt D (2003) Scale-resolved electrochemical surface structuring of titanium for biological applications. J Electrochem Society 150(11):B495

37. Yi R, Zhang Y, Zhang X, Fang F, Deng H (2020) A generic approach of polishing metals via isotropic electrochemical etching. Int J Mach Tools Manuf 150:103517

38. Madore C, Landolt D (1997) Electrochemical micromachining of controlled topographies on titanium for biological applications. J Micromech Microeng 7:270–275

39. Chauvy PF, Hoffmann P, Landolt D (2003) Applications of laser lithography on oxide film to titanium micromachining. Appl Surf Sci 208–209:165–170

40. Lu X, Leng Y (2005) Electrochemical micromachining of titanium surfaces for biomedical applications. J Mater Process Technol 169:173–178

41. Yu Y, Shironita S, Souma K, Umeda M (2018) Effect of chromium content on the corrosion resistance of ferritic stainless steels in sulfuric acid solution. Heliyon 4:e00958

42. Toušek J (1977) Electropolishing of metals in alcoholic solution of sulphuric acid. Electrochim Acta 22:47–50

43. Han W, Fang FZ (2020) Investigation of electropolishing characteristics of tungsten in eco-friendly sodium hydroxide aqueous solution. Adv Manuf 8:265–278

44. Yuan W, Li L-H, Lee W-B, Chan C-Y (2018) Fabrication of microlens array and its application: a review. Chin J Mech Eng 31(1):1–9